Appl. Phys. A (2016) 122:783
DOI 10.1007/s00339-016-0296-0

Applied Physics A
Materials Science & Processing

Large controllability of domain evolution in ferroelectric nanodot via isotropic surface charge screening

W. M. Xiong[1,2] · Qiang Sheng[1,2,3] · W. J. Chen[1,2] · C. M. Wu[1,2] · Biao Wang[1,2] · Yue Zheng[1,2]

Received: 24 November 2015 / Accepted: 21 July 2016 / Published online: 2 August 2016

Abstract This work reports a large controllability of domain evolution in $BaTiO_3$ ferroelectric nanodot by isotropic surface charge screening (SCS). The phase field simulations show that the nanodot can exhibit fruitful domain patterns and evolution paths as functions of temperature and screening factor and changing direction of these two variables. Four typical types of experimental processes have been simulated, including the cooling-down and heating-up processes under fixed SCS conditions, and the processes of increasing and decreasing SCS under fixed temperatures. During these processes, the nanodot exhibits up to 13 different kinds of domain patterns, among which some are either polar or toroidal and some are both polar and toroidal. We summarized the phase diagrams as functions of temperature and charge screening factor, and also analyzed the typical domain evolution paths.

✉ Yue Zheng
zhengy35@mail.sysu.edu.cn

Biao Wang
wangbiao@mail.sysu.edu.cn

[1] State Key Laboratory of Optoelectronic Materials and Technologies, School of Physics and Engineering, Sun Yat-sen University, 510275 Guangzhou, China

[2] Micro & Nano Physics and Mechanics Research Laboratory, School of Physics and Engineering, Sun Yat-sen University, 510275 Guangzhou, China

[3] Materials Science and Engineering Department, Harbin Institute of Technology Shenzhen Graduate School, 518055 Shenzhen, China

1 Introduction

Due to the collective nature of ferroelectricity and its interplay with surface or interface, the polarization stability and the formation of domain structure of ferroelectric materials are sensitive to the surrounding environments. In the literature, it has been known for a long time that the incomplete screening of surface polarization charges contributes a depolarization field inside the ferroelectrics. This depolarization field can largely depress the ferroelectricity and leads to the appearance of critical size, below which the system loses its ferroelectricity [1–3]. Also due to the depolarization field, monodomain state is difficult to maintain in the ferroelectrics; instead, polydomain structures are usually formed [4–6].

Conventionally, people use electrodes to screen the surface polarization charges. By choosing the electrodes with good screening ability, it has been shown that ferroelectricity can maintain stability in several unit-cell epitaxial thin films [7–10]. Recently, more strategies have been proposed to screen the surface polarization charges of ferroelectrics. For example, Fong et al. [11] reported that monodomain state can maintain in 1.2-nm $PbTiO_3$ ultrathin film which is exposed in a controlled vapor environment. Interestingly, they further showed that the domain state can be switched by controlling the oxygen partial pressure via either a nucleation mode or a continuous mode without nucleation [12]. Shin et al. [13] investigated the ultrathin $BaTiO_3$ films exposed to water molecules and found that water vapor exposures can result in surface hydroxylation and rippling, formation of surface oxygen vacancies, and reversal of the polarization direction. Using oxygen plasma, Kim et al. [14] also reported reversible polarization switching in epitaxial $BiFeO_3$ thin films. These works indicate that controlling the surface chemical environment

of the ferroelectric is also a promising method to control the ferroelectric stability and the evolution of ferroelectric domain structure.

Recently, ferroelectric nanostructures have attracted intensive academic attentions. This is not only due to the prospect of maintaining remarkable bulk properties at nanoscale, but also due to that the complex surface and interface effects provide us a possibility of achieving novel or abnormal properties from those of bulk counterparts. Particularly, vortex domain structure (VDS), a special type of domain structure with toroidal polar domains, can appear in ferroelectric nanostructures under near open-circuit boundary conditions [15]. Because of its distinctive characteristics and novel coupling with external fields, ferroelectric VDS has been under active investigations [16–24]. For example, based on an effective Hamiltonian approach, it has been shown that not only the chirality of single-vortex state in asymmetric nanorings but also that of double-vortices state in prolate nanosystems can be reversed by a homogeneous electric field [18, 19]. Based on phase field simulations, some novel strategies for the control of VDS properties such as its size, orientation and transformation via mechanical loads [22, 24] and proper geometry design of the system [23] have also been revealed.

The mechanism of forming VDS in ferroelectric nanostructures is to avoid the large depolarization field caused by the exposed surfaces. According to the previous works on ferroelectric thin films [12, 14, 25–28], controlling the surface environment such as surface charge screening (SCS) of the ferroelectrics should also be effective to control the VDS. Previous investigations have indeed shown that the formation of VDS is sensitive to the SCS condition [16, 21]. Nevertheless, in these works, the effect of SCS was explored by treating SCS as a fixed electrical boundary condition, and the VDS formation from random noise was focused. Investigations treating SCS as a control variable to induce the evolution and transformation of existent VDSs similar to those done in thin film systems [12–14] are scarce. Recently, Wu et al. [29, 30] investigated the effect of variable SCS condition on existent VDS in ferroelectric nanodots. Their simulated results showed that fruitful vortex domain patterns and evolution paths can be induced by varying the SCS condition. It is noteworthy that in their investigation the SCS was applied to the nanodots along a specific direction. Such kind of SCS condition is highly anisotropic.

In this paper, we make a further investigation on the combining effects of SCS condition and temperature on the formation and evolution of domain patterns in $BaTiO_3$ (BTO) nanodot. The ferroelectric nanodot is supposed to be placed in a chemical environment of charged gas molecules. Being different with previous works [29, 30], an isotropic SCS condition is applied to the nanodot. For this condition, the surface polarization charges on all the surfaces of the nanodot are compensated by absorbed charged gas molecules. Using a phase field method, we systematically simulate four typical types of experimental processes, including the cooling-down and the heating-up processes under fixed SCS conditions, and the processes of increasing and decreasing screening extent under fixed temperatures. The phase diagrams of equilibrium domain patterns are summarized as functions of SCS factor and temperature. We also analyze the domain evolution paths induced by the varying SCS and temperature.

2 The physical model

In our work, a phase field model is adopted to simulate the domain structure evolution in ferroelectric nanodots under SCS condition. The spontaneous polarization $\mathbf{P} = (P_1, P_2, P_3)$ is considered as the order parameter. The total polarization of a ferroelectric can be divided into the linear and the nonlinear terms. The temporal evolution of the spontaneous polarization in a ferroelectric nanodot is calculated by solving the time-dependent Ginzburg–Landau (TDGL) equations, i.e., $\partial P_i/\partial t = -M\delta F/\delta P_i\,(i = 1, 2, 3)$,where M is the kinetic coefficient related to the domain wall mobility, F is the total free energy, t is time. To include the effects of inhomogeneous electromechanical fields and surface, the total free energy in the ferroelectric nanodot is expressed as $F = \int_V (f_{\text{Land}} + f_{\text{grad}} + f_{\text{elas}} + f_{\text{elec}})\mathrm{d}V + \int_S f_{\text{surf}}\mathrm{d}S$,where f_{Land}, f_{grad}, f_{elas}, f_{elec} and f_{surf} are the densities of Landau free energy, gradient energy, elastic energy, electric energy and surface energy, respectively. V and S are the volume and surface of the nanodot, respectively.

The Landau free energy density f_{Land} describes the free energy of bulk material. By expanding it to an eighth-order polynomial, f_{Land} is written as [31, 32],

$$\begin{aligned} f_{\text{Land}} = {} & \alpha_1 \sum_i P_i^2 + \alpha_{11} \sum_i P_i^4 + \alpha_{12} \sum_{i>j} P_i^2 P_j^2 + \alpha_{111} \sum_i P_i^6 \\ & + \alpha_{112} \sum_{i>j} \left(P_i^4 P_j^2 + P_j^4 P_i^2 \right) + \alpha_{123} \prod_i P_i^2 + \alpha_{1111} \sum_i P_i^8 \\ & + \alpha_{1112} \sum_{i>j} \left(P_i^6 P_j^2 + P_j^6 P_i^2 \right) + \alpha_{1122} \sum_{i>j} P_i^4 P_j^4 + \alpha_{1123} \\ & \sum_{i \neq j \neq k, j>\mathrm{k}} P_i^4 P_j^2 P_k^2 \end{aligned} \tag{1}$$

where α_1 is the temperature-dependent dielectric stiffness satisfying the Curie–Weiss relation, and α_{ij}, α_{ijk} and α_{ijkl} are the higher-order dielectric stiffness coefficients.

The gradient energy density f_{grad} can be expressed by the gradients of the polarization field and it describes the free

energy contributed by the spatial polarization variation in the material. Since the background material is cubic crystal structure, the lowest order Taylor expansion of the gradient energy density f_{grad} can be written as follow,

$$\begin{aligned} f_{\text{grad}}(P_{i,j}) &= \frac{1}{2}G_{11}\sum_i P_{i,i}^2 + G_{12}\sum_{i>j} P_{i,i}P_{j,j} \\ &\quad + \frac{1}{2}G_{44}\sum_{i>j}(P_{i,j}+P_{j,i})^2 + \frac{1}{2}G'_{44}\sum_{i>j}(P_{i,j}-P_{j,i})^2 \\ &= \frac{1}{2}G_{11}\left(P_{1,1}^2+P_{2,2}^2+P_{3.3}^2\right) \\ &\quad + G_{12}(P_{1,1}P_{2,2}+P_{2,2}P_{3,3,}+P_{1,1}P_{3,3}) \\ &\quad + \frac{1}{2}G_{44}[(P_{1,2}+P_{2,1})^2+(P_{2,3}+P_{3,2})^2 \\ &\quad + (P_{1,3}+P_{3,1})^2)] + \frac{1}{2}G'_{44}[(P_{1,2}-P_{2,1})^2 \\ &\quad + (P_{2,3}-P_{3,2})^2+(P_{1,3}-P_{3,1})^2)] \end{aligned} \tag{2}$$

where G_{11}, G_{12}, G_{44} and G'_{44} are gradient energy coefficients, and the comma in the subscript denotes spatial differentiation.

Ferroelectric phase transition involves structural changes, which lead to the appearance of spontaneous strain $\varepsilon_{ij}^0 = Q_{ijkl}P_kP_l$. Thus, the mechanical strain field and its coupling with polarization contribute to the elastic energy density f_{elas}, which can be expressed by,

$$\begin{aligned} f_{\text{elas}} &= {}^1\!/\!_2 c_{ijkl}e_{ij}e_{kl} = {}^1\!/\!_2 c_{ijkl}(\varepsilon_{ij}-\varepsilon_{ij}^0)(\varepsilon_{kl}-\varepsilon_{kl}^0) \\ &= {}^1\!/\!_2 C_{11}[(\varepsilon_{11}-\varepsilon_{11}^0)^2+(\varepsilon_{22}-\varepsilon_{22}^0)^2+(\varepsilon_{33}-\varepsilon_{33}^0)^2] \\ &\quad + C_{12}[(\varepsilon_{22}-\varepsilon_{22}^0)(\varepsilon_{33}-\varepsilon_{33}^0)+(\varepsilon_{11}-\varepsilon_{11}^0)(\varepsilon_{33}-\varepsilon_{33}^0) \\ &\quad + (\varepsilon_{11}-\varepsilon_{11}^0)(\varepsilon_{22}-\varepsilon_{22}^0)] \\ &\quad + 2C_{44}[(\varepsilon_{23}-\varepsilon_{23}^0)^2+(\varepsilon_{13}-\varepsilon_{13}^0)^2+(\varepsilon_{12}-\varepsilon_{12}^0)^2] \end{aligned} \tag{3}$$

where c_{ijkl} and C_{ij} are the fourth-order and reduced elastic coefficients, $e_{ij} = \varepsilon_{ij} - \varepsilon_{ij}^0$ is the elastic strain and ε_{ij} is the total strain. The total strain ε_{ij} is related to the displacement u_i and is described as $\varepsilon_{ij} = {}^1\!/\!_2(u_{i,j}+u_{j,i})$, where the comma in the subscript denotes spatial differentiation. In order to calculate the displacement field, the mechanical equilibrium equations $\sigma_{ij,j}\big|_V = c_{ijkl}(\varepsilon_{kl}-\varepsilon_{kl}^0)_{,j}\Big|_V = 0$ are solved with the stress-free boundary conditions $\sigma_{ij}n_j = 0$, where n_j is the j-component of the unit vector normal to the surface.

The polarization is inhomogeneous near the truncated surfaces. To capture this effect, it is necessary to consider a surface energy. The surface energy density can be expressed in the following form, i.e., $f_{\text{surf}} = \sum_i D_i^{\text{S}}P_i^2/2\delta_i^{\text{eff}}$, where δ_i^{eff} are the extrapolation lengths [1], D_i^{S} are the coefficients related to the gradient energy coefficients and surface orientation. In detail, $D_1^{\text{S}} = G_{11}n_1 + (G_{44}+G'_{44})(n_2+n_3)$, $D_2^{\text{S}} = G_{11}n_2 + (G_{44}+G'_{44})(n_1+n_3)$ and $D_3^{\text{S}} = G_{11}n_3 + (G_{44}+G'_{44})(n_1+n_2)$ [33], where n_i is the component of unit vector normal to the surfaces. Moreover, the extrapolation length which is contained in the surface energy is introduced to characterize the difference in polarization between the surface and the interior of the material. When the extrapolation length is positive, the polarization is reduced at the surface. And the polarization is enhanced at the surface when the extrapolation length is negative. When the extrapolation length equals zero, the polarization is suppressed and the polarization is zero at the surface. When the extrapolation length approaches infinity, there is no difference in polarization between the surface and the interior and the surface effect will vanish. Actually, the extrapolation lengths depend on the polarization state. Nevertheless, for simplicity and due to the lacking knowledge of such dependence, we take extrapolation lengths as constants, as what was done in most of the existing phase field models [29, 30].

Since the background material is the paraelectric phase of a cubic crystal structure, the background dielectric constants along the axis directions are the same. The electric energy density f_{elec} is written as $f_{\text{elec}} = -\sum_i P_iE_i - {}^1\!/\!_2\varepsilon_b\sum_i E_iE_i$ [34, 35]. In our case, we do not consider external electric field and suppose that free charge does not exist inside the nanodot. The maximum and minimum depolarization field distributions E^{OC} and E^{SC} are obtained by solving the electrostatic equilibrium equation with appropriate boundary conditions. Specifically, when the nanodot is under open-circuit condition, the depolarization field is induced by inhomogeneous spontaneous polarizations and uncompensated polarization surface charges. We obtain the depolarization field E^{OC} by solving the electrostatic equilibrium equation $\text{D}_{i,i} = (\varepsilon_0\boldsymbol{\kappa}\text{E}+\text{P})_{i,i} = 0$ under the ideal open-circuit boundary condition $D_in_i = 0$ [30], where ε_0 is the dielectric constant of vacuum and $\boldsymbol{\kappa}$ denotes the relative dielectric constants of the material and n_i is the component of unit vector normal to the surfaces. When the nanodot is under short-circuit condition, the surface charge is screened and the depolarization field $\mathbf{E}^{\mathbf{SC}}$ is only induced by inhomogeneous spontaneous polarizations. We solve the electrostatic equilibrium equation $\text{D}_{i,i} = (\varepsilon_0\boldsymbol{\kappa}\text{E}+\text{P})_{i,i} = 0$ under the ideal short-circuit boundary condition $\phi = 0$ [36]. Moreover, the nanodot is placed to a chemical environment. The surface polarization charges on the surfaces of nanodot are compensated by the charged gas molecules. The depolarization field in the nanodot can be controlled by the extent of SCS through changing the surrounding environment. We approximate the extent of

SCS along the three directions by screening factors β_i ($i = 1, 2, 3$), so that the depolarization field inside the nanodot can be calculated by $\mathbf{E} = \beta_i \mathbf{E}^{OC} + (1 - \beta_i)\mathbf{E}^{SC}$ [30], where $\mathbf{E}^{OC}$ and $\mathbf{E}^{SC}$ are the depolarization field under ideal OC ($\beta_i = 1$) and SC ($\beta_i = 0$) conditions, respectively. For an isotropy SCS condition, we always keep $\beta_1 = \beta_2 = \beta_3 = \beta$. By varying the value of β between one and zero, different extent of isotropic SCS can be simulated.

In the simulations, the TDGL equations are solved using the explicit finite difference method, and the mechanical and electrostatic equilibrium equations are solved by the finite element method. Values of the expansion coefficients of the eighth-order Landau–Devonshire potential, electrostrictive coefficients, elastic properties [32, 37, 38] and extrapolation length [39] in the simulations are listed in Ref. [40].

3 Results and discussions

In the simulations, we employ a 10 × 10 × 10 meshing at a scale of $\Delta x = \Delta y = \Delta z = 0.4$ nm to model a 4 nm × 4 nm × 4 nm BTO nanodot. We explore the combining effects of isotropic SCS condition and temperature on the domain structure evolution of the nanodot, as schematically shown in Fig. 1. The study includes four typical types of experimental processes, i.e., the (i) cooling-down (CD) and (ii) heating-up (HU) processes at fixed SCS conditions, and the processes of (iii) increasing and (iv) decreasing SCS at fixed temperatures. We first start the simulation of CD processes. A random distribution of polarization field is used to initiate the polarization evolution at high temperature and fixed SCS conditions (β ranging from 0 to 1). As the temperature decreases below the paraelectric–ferroelectric transition temperature, a stable domain pattern is obtained and is used as the initial domain pattern for next temperature step. The stable domain patterns obtained at $T = 0$ K at different SCS conditions are further used as the initial domain patterns for the HU processes. Moreover, the stable domain patterns obtained in CD processes under the ideal OC ($\beta = 1$) and SC ($\beta = 0$) conditions are also used as the initial domain patterns for the processes of increasing (β changes from 1 to 0) and decreasing SCS (β changes from 0 to 1) at fixed temperatures, respectively. Domain patterns are characterized by plotting their detailed morphologies and also by calculating the average polarization $\overline{\mathbf{P}}$ and the toroidal moment $\mathbf{g} = \frac{1}{V}\int_V \mathbf{r} \times (\mathbf{P} - \overline{\mathbf{P}})\mathrm{d}V$ [41], where $\mathbf{r}$ is the position vector. To clearly capture the domain transformations, we also calculate the average magnitude of polarization at all the sites, i.e., $<P> = \mathrm{mean}(\sqrt{P_1^2 + P_2^2 + P_3^2})$. Note, to have a clear reference to different domain patterns, we label each domain pattern with a specific symbol throughout this paper, and the detailed domain morphologies are shown in Figs. 2, 3 and 5.

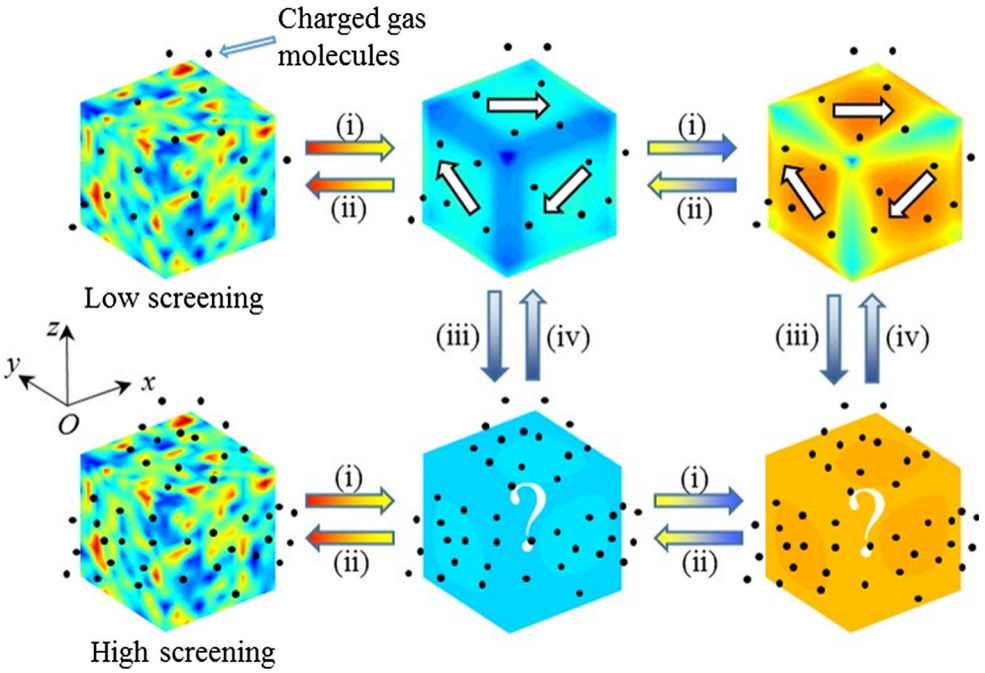

Fig. 1 Schematics of how the domain structure of a ferroelectric nanodot may evolve during various isotropic surface charge screening (SCS) processes. Processes (**i**) and (**ii**) are the cooling-down and heating-up processes at fixed surface charge screening, respectively. Processes (**iii**) and (**iv**) are the processes of increasing (from $\beta = 1$ to $\beta = 0$) and decreasing (from $\beta = 0$ to $\beta = 1$) surface charge screening at fixed temperature, respectively

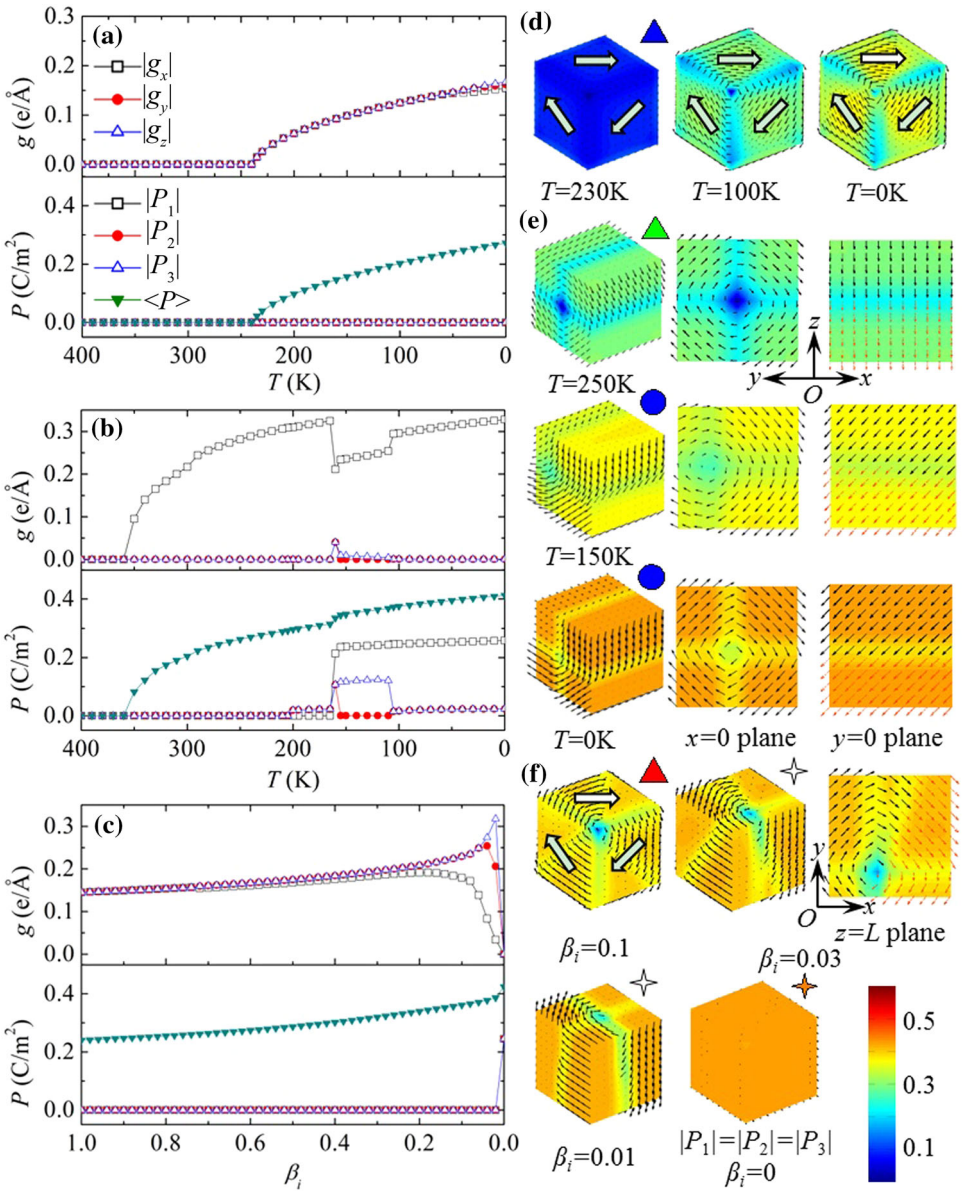

Fig. 2 Simulated domain evolution of a ferroelectric nanodot under typical SCS processes. **a** Toroidal moment, polarization and (**d**) evolved domain patterns of the nanodot during a cooling-down process under open-circuit boundary condition ($\beta = 1$), **b** Toroidal moment, polarization and (**e**) evolved domain patterns of the nanodot during a cooling-down process under near short-circuit boundary condition ($\beta = 0.02$). **c** Toroidal moment, polarization and (**f**) evolved domain patterns of the nanodot during increasing surface charge screening (from $\beta = 1$ to $\beta = 0$) at $T = 50$ K

3.1 First insight into the effect of SCS on the domain structure formation and evolution

We would like to gain a first insight into the effect of SCS on the domain structure formation and evolution in BTO nanodot by the results shown in Fig. 2. Specifically, in Fig. 2a, d we depict the domain evolution of the nanodot during a CD process under the ideal OC ($\beta = 1$) condition. In Fig. 2b, e we depict the domain evolution of the nanodot during a CD process under a near SC ($\beta = 0.02$) condition. From the polarization and toroidal moment curves plotted in Fig. 2a, one can see that during the process both the polarization and toroidal moment become nonzero at a temperature of about 235 K, indicating that the paraelectric–ferroelectric transition happens at this temperature and a vortex domain pattern is formed in the nanodot. From the magnitude of the toroidal moment components and the domain morphologies shown in Fig. 2d, we can clearly see that the vortex domain pattern is rhombohedral (i.e., $|g_x| = |g_y| = |g_z|$, labeled by blue triangle). This vortex domain pattern has been predicted in previous works [29, 30]. As temperature further decreases, the polarization and toroidal moment smoothly increase and the rhombohedral vortex state (blue triangle) keeps stable in the nanodot. For the CD process under near SC condition as shown in Fig. 2b, e the domain evolution of the nanodot is quite different from that under the OC condition. The paraelectric–ferroelectric transition happens at a much higher temperature of about 350 K. Moreover, the vortex domain pattern formed near the paraelectric–ferroelectric transition

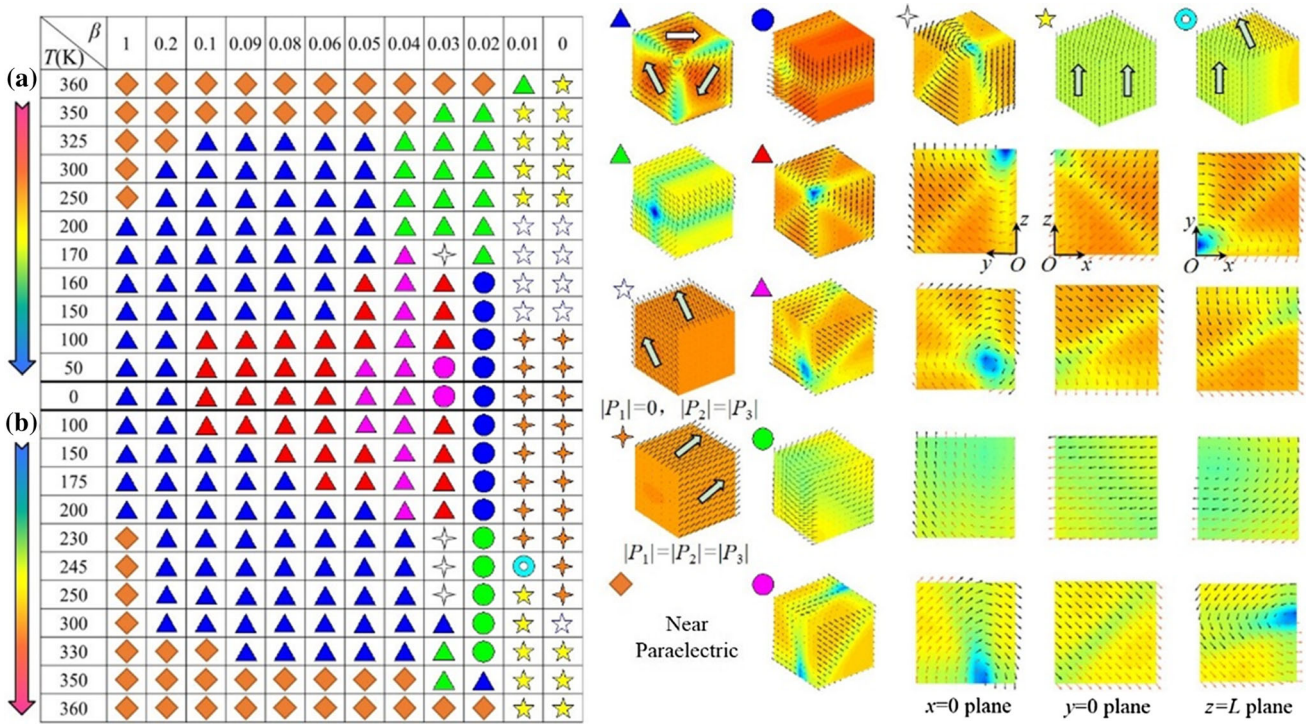

Fig. 3 Phase diagrams of equilibrium domain pattern as a function of temperature and charge screening of a ferroelectric nanodot during the processes of **a** cooling-down and **b** heating-up under different surface charge screening conditions

is tetragonal (i.e., $|g_x| \neq 0$, $|g_y| = |g_z| = 0$) (see the domain morphology at $T = 250$ K in Fig. 2e). With the decrease in temperature, toroidal moment $|g_x|$ and average polarization magnitude $<P>$ increase gradually, while the other components keep null. As temperature reaches about 160 K, abrupt changes in the toroidal moment and polarization are observed, indicating a change in the domain pattern. This is verified by the domain morphology of the nanodot at $T = 150$ K as shown in Fig. 2e, where the vortex core is no longer across the center of x-surface but shifts to the side surface. Specifically, this domain pattern (labeled by blue circle) has a toroidal moment along the x-axis and also has nonzero x and z polarization components. This vortex domain pattern keeps stable until the temperature further reduces to $T = 105$ K. Around $T = 105$ K, $|g_x|$ has an abrupt increase, and $|P_3|$ drops to null. Analyzing the domain patterns at the low temperature region ($0 \sim 105$ K), we found that the vortex state is similar to the previous one (thus we also label it by blue circle for simplicity), with the vortex core shifting back to the center of x-surface (see the domain morphology at $T = 0$ K in Fig. 2e). Comparing the results of the OC condition and the near SC condition, one can see that the SCS condition indeed largely affects the formation of VDS during CD processes. Interestingly, the results show that the paraelectric–ferroelectric transition temperature is in the range of several hundred K under different screening conditions. According to previous works [26, 30], we also can find that the surface charge screening has large impact on the paraelectric–ferroelectric transition temperature. In the Ref. [26], the phase diagrams as a function of oxygen pressure and temperature for the ferroelectric thin films are summarized. Actually, the screening extent of surface polarization charges can be controlled by the oxygen pressure. From the phase diagrams, the paraelectric–ferroelectric transition also occurs during a large range of several hundred K under different oxygen pressure.

Moreover, Fig. 2c depicts the domain evolution of the nanodot during the process of increasing SCS at $T = 50$ K. The domain morphologies at selected temperatures are depicted in Fig. 2f. From the toroidal moment and polarization curves shown in Fig. 2c, one can see that the rhombohedral vortex domain pattern (blue triangle) forms in the nanodot under low SCS conditions ($\beta > 0.3$). With an increase in SCS ($\beta < 0.3$), $|g_y|$ and $|g_z|$ keep equal and increase gradually, while $|g_x|$ gradually decreases, indicating the slight change in the vortex domain pattern. As β further decreases ($\beta < 0.03$), two of the toroidal moment components ($|g_x|$ and $|g_y|$) decrease rapidly, meanwhile the rest one ($|g_z|$) first increases an amount and then also decreases rapidly. Finally, all toroidal moment components drop to null at $\beta = 0$. At this condition, the polarization components also become nonzero and equal to each other. From the domain morphologies shown in Fig. 2f, during

the process of increasing SCS, the axis of vortex core gradually tilts from <111> direction to in-plane, leading to the appearance of a distorted rhombohedral vortex state (labeled by hollow four-pointed star) as the screening factor smaller than 0.3. Lastly, a r single-domain state ($|g_x| = |g_y| = |g_z| = 0$, $|P_1| = |P_2| = |P_3| \neq 0$, labeled by solid four-pointed star) forms because of the complete compensation of the surface polarization charges.

3.2 Phase diagrams and evolution of domain patterns during CD and HU processes

In Fig. 3, the equilibrium domain patterns observed in the nanodot during CD and HU processes are summarized by phase diagrams as functions of the SCS factor and temperature. Overall, twelve types of domain patterns (note, the classification is not rigorous) are observed in the simulations. Rhombohedral vortex domain pattern (blue triangle) favors to form under low SCS conditions ($\beta > 0.1$). If the surface polarization charges are completely compensated, c single-domain state (i.e., $|g_x| = |g_y| = |g_z| = 0$, $|P_1| = |P_2| = 0$, $|P_3| \neq 0$, yellow pentagram in the phase diagram) is stable under low temperatures and r single-domain state (solid four-pointed star) forms under high temperatures. To be more detailed, under the condition of $\beta > 0.1$, the rhombohedral vortex state forms in the nanodot near the paraelectric–ferroelectric transition temperature during the CD process, and this state maintains stability until temperature decreases to $T = 0$ K. Interestingly, similar domain patterns and evolution paths are obtained during the HU process. The paraelectric–ferroelectric transition temperatures are nearly the same during the CD and HU processes, indicating a second-order feature of the phase transition. Moreover, the paraelectric–ferroelectric transition temperature increases with the increase in SCS. These results are in consistence with those of the previous works [30].

With a further increase in SCS (i.e., $0.06 \leq \beta \leq 0.1$), the rhombohedral vortex state (blue triangle) forms in the nanodot right below the paraelectric–ferroelectric transition point. When temperature decreases to near $T = 100$ K, the axis of vortex core would deviate from the <111> direction a little bit, indicating the formation of an orthorhombic-like vortex state (red triangle in the phase diagram). This vortex state maintains stability until temperature decreases to $T = 0$ K. During the HU process, the vortex core of the initial orthorhombic-like vortex state gradually shifts back to <111> direction with the increase in temperature, leading to the re-formation of the rhombohedral vortex state. Comparing the evolution paths under these SCS conditions, we can see that the transition temperature increases gradually with the increase in SCS in the HU process. When SCS increases to $\beta = 0.05$, the rhombohedral vortex state forms at $T = 325$ K, and the orthorhombic-like vortex state is stable when temperature decreases to $T = 160$ K. With a further decrease in temperature to $T = 50$ K, the axis of vortex core has a large deviation from <111> direction. At this temperature, the domain pattern is a tetragonal-like vortex state (pink triangle) with the vortex core lying in y–z plane. The domain pattern is stable until temperature decreases to $T = 0$ K. In the HU process, the axis of vortex core of the initial tetragonal-like vortex state gradually shifts to the <111> direction with the increase in temperature. When temperature increases to $T = 200$ K, the rhombohedral vortex state reforms in the nanodot.

With a further increase in SCS ($0.02 \leq \beta \leq 0.04$), the domain patterns and evolution paths are even more abundant. Under these SCS conditions, the tetragonal vortex state (green triangle) forms near the paraelectric–ferroelectric transition temperature. With the decrease in temperature, the vortex core shifts from the center of y–z plane to the vertex of the nanodot under $\beta = 0.04$ and $\beta = 0.03$. Under the condition of $\beta = 0.04$, a vortex domain pattern with its vortex core keeping a distance from the vertex is formed throughout the CD process (see the pink triangle in the phase diagram). The evolution path under the condition of $\beta = 0.03$ is more complex. The vortex core of the domain pattern shifts to the position near the vertex of the nanodot at $T = 170$ K. As temperature decreases to $T = 50$ K, the vortex core is at the edge of the nanodot, indicating the forming of a new vortex domain pattern (pink circle in the phase diagram). During the HU process at $\beta = 0.04$, the vortex domain pattern (pink triangle) directly transforms to the rhombohedral vortex state (blue triangle) at $T = 230$ K, without the observation of the tetragonal vortex state (green triangle). In contrast, in the evolution of $\beta = 0.03$, the vortex core shifts from the edge to the vertex of the nanodot with the increase in temperature. As temperature reaches 300 K, the rhombohedral vortex state (blue triangle) forms in the nanodot. And at higher temperatures, the rhombohedral vortex state (blue triangle) transforms into the tetragonal vortex state (green triangle). The detailed evolution path under the condition of $\beta = 0.02$ is depicted in Fig. 2 and discussed above.

As SCS further increases to $\beta \leq 0.01$, single-domain states favor to form in the nanodot. During the CD process at $\beta = 0.01$, the nanodot first adopts a tetragonal vortex state (green triangle) near the paraelectric–ferroelectric transition temperature ($\sim$360 K). This tetragonal vortex state (green triangle) would transform into a c single-domain state (yellow pentagram) at lower temperature ($\sim$350 K). Meanwhile, during the CD process at the ideal SC condition ($\beta = 0$), c single-domain state directly forms

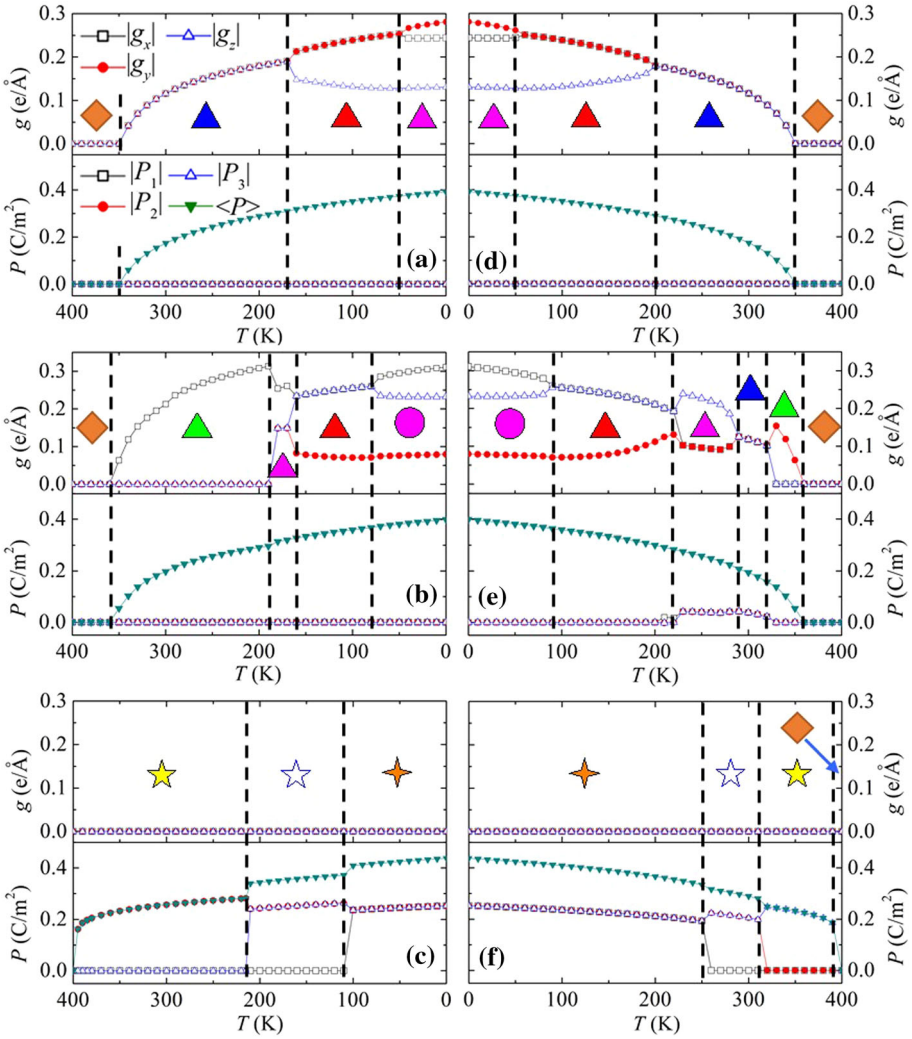

Fig. 4 Evolution of the toroidal moment, polarization and domain pattern of a nanodot during a cooling-down process under typical high SCS conditions of **a** $\beta = 0.05$, **b** $\beta = 0.03$ and **c** $\beta = 0$, and during a heating-up process under the condition of **d** $\beta = 0.05$, **e** $\beta = 0.03$ and **f** $\beta = 0$

at the paraelectric–ferroelectric transition point ($\sim$360 K). For both SCS conditions ($\beta = 0.01$ and $\beta = 0$), *c* single-domain state would further transforms into *ac* single-domain state (i.e., $|g_x| = |g_y| = |g_z| = 0$, $|P_1| = 0$, $|P_2|$ and $|P_3| \neq 0$, white pentagram) at the temperature range of 150 K $< T <$ 200 K. With a further decrease in temperature ($T <$ 150 K), the *r* single-domain state (solid four-pointed star) becomes stable in the nanodot. During the HU processes at $\beta = 0.01$ and $\beta = 0$, the domain pattern evolves with the disappearance of in-plane polarization during the process of increasing temperature. Lastly, *c* single-domain state reforms in the nanodot under a high temperature.

From the phase diagrams of CD and HU processes discussed above, one can see that abundant domain patterns and evolution paths can be obtained by varying the SCS condition and temperature. Such controllability is especially large near high SCS condition. In order to see clearly the evolution paths under high SCS conditions, three specific SCS conditions (i.e., $\beta = 0.05, 0.03$ and 0) are depicted in Fig. 4. During the CD process under the condition of $\beta = 0.05$ (see Fig. 4a), the toroidal moment components and average polarization magnitude $<P>$ become nonzero at the paraelectric–ferroelectric transition temperature of about 350 K. With the decrease in temperature, all the toroidal moment components keep equal and the polarization keeps null, indicating the rhombohedral vortex state (blue triangle) forms in the nanodot. Then, the toroidal moment components and average polarization magnitude $<P>$ increase with the decrease in temperature. As temperature lies in the range of 50 K $< T <$ 170 K, $<P>$ continuously increases, while $|g_x|$ and $|g_y|$ keep equal and are larger than $|g_z|$, indicating the formation of orthorhombic-like vortex state (red triangle). As temperature decreases below 50 K, curves of the toroidal moment components no longer coincide with each other (i.e., $|g_y| > |g_x| > |g_z|$). It indicates that a vortex state (pink triangle) with the toroidal moment components differing in magnitudes forms in the nanodot. As a contrast, a reverse evolution path during the HU process is depicted in Fig. 4d. The same domain patterns have been observed in

this process. Comparing the CD and HU processes, one can also see that the ferroelectric–paraelectric transition temperatures as well as the transformation temperatures between the vortex state (pink triangle) and the orthorhombic-like state (red triangle) are almost the same for the two processes. Meanwhile, the transform temperatures at which the domain pattern transforms between the orthorhombic-like state (red triangle) and rhombohedral vortex state (blue triangle) are quite different during the two processes. We found $T = 200$ K in the HU process, which is larger than the temperature of 170 K in the CD process. This indicates a first-order feature of this domain structure transformation.

As shown in Fig. 4b and e, four and five domain patterns are obtained in the CD and HU processes under the condition of $\beta = 0.03$, respectively. In the CD process, the tetragonal vortex state (green triangle) forms when paraelectric–ferroelectric transition occurs. With the decrease in temperature in the range of 360 K $> T >$ 190 K, $|g_x|$ and $<P>$ keep increasing. When temperature decreases to $T = 190$ K, $|g_y|$ and $|g_z|$ increase suddenly to nonzero values of about 0.15 e/Å, while $|g_x|$ has a decrease from 0.31 to 0.25 e/Å, indicating the formation of a tetragonal-like vortex state (pink triangle). This state maintains only within 160 K $< T <$ 190 K. With a further decrease in temperature, $|g_z|$ becomes equal to $|g_x|$, while $|g_y|$ decreases and keeps a value of $\sim$0.05 e/Å in the temperature range of 80 K $< T <$ 160 K. In this temperature range, the nanodot adopts an orthorhombic-like vortex state (red triangle). As temperature decreases to range of $T < 80$ K, $|g_x|$ and $|g_z|$ become unequal, and the three components change only slightly with the temperature, indicating the formation of a new vortex domain pattern (pink circle). In the reverse HU process, the domain evolution is more complex. When temperature increases from 0 to 90 K, the difference between the $|g_x|$ and $|g_z|$ gradually decreases, and they become equal at 90 K. It indicates that the orthorhombic-like vortex state (red triangle) reforms in the nanodot. This vortex state maintains stability at T between 90 and 215 K, with $|g_x|$ and $|g_z|$ gradually decreasing and $|g_y|$ increasing. Domain pattern of the nanodot transforms from orthorhombic-like vortex state (red triangle) to tetragonal-like vortex state (pink triangle) at $T = 220$ K. With a further increase in temperature ($T > 220$ K), the evolution of domain pattern in the HU process is different from the one in the CD process. Rhombohedral vortex state (blue triangle) is observed in the region of T between 220 and 315 K. When temperature increases to 315 K, the rhombohedral vortex state transforms into tetragonal vortex state (green triangle). Near the ferroelectric–paraelectric transition temperature, the toroidal moment components and polarization components become null, indicating that paraelectric phase reforms in the nanodot.

Figure 4c and f depicts the domain evolution paths of the nanodot during the CD and HU processes under ideal SC condition, respectively. *c* single-domain state (yellow pentagram) forms when paraelectric–ferroelectric transition happens. With a further decrease in temperature (395 K $> T >$ 215 K), $|P_2|$ increases and the *c* single-domain state maintains in the nanodot. At $T = 215$ K, $|P_2|$ and $|P_3|$ become equal. This indicates that the domain pattern of the nanodot transforms from the *c* single-domain state (yellow pentagram) to the *ac* single-domain state (white pentagram). The *ac* single-domain state maintains in the nanodot at T between 215 and 110 K. When temperature decreases to $\sim$100 K, $|P_1|$ has an abrupt increase and the three polarization components become equal to each other. This reflects that *r* single-domain state (solid four-pointed star) forms in the nanodot. With a further decrease in temperature ($T < 100$ K), the *r* single-domain state maintains stability in the nanodot. In the reverse HU process, the *r* single-domain keeps stable in the nanodot at 0 K $< T <$ 250 K. When temperature reaches 260 K, $|P_1|$ drops to null, while $|P_2|$ and $|P_3|$ both increase a little bit. At this point, the *r* single-domain state transforms into the *ac* single-domain state. With a further increase in temperature (260 K $< T <$ 310 K), the *ac* single-domain state (white pentagram) is stable in the nanodot. When temperature increases to 320 K, $|P_2|$ drops to null and $|P_3|$ increases a little bit, indicating that the *c* single-domain state (yellow pentagram) forms in the nanodot. And this *c* single-domain state maintains stability in the nanodot at the temperature between 320 and 390 K. With a further increase in temperature, the polarization becomes null near 390 K, indicating that paraelectric phase reforms in the nanodot. In the HU process, the temperatures of *r*-*ac* and *ac*-*c* transformations are 250 and 310 K, respectively, which are larger than the ones of 110 and 220 K in the CD process. It indicates a first-order feature of these transformations in the nanodot.

Comparing the phase diagrams in Fig. 3 with the previous works [29, 30], we observe some similar domain patterns and evolution paths. Particularly, the rhombohedral vortex state (blue triangle) forms in the nanodot under low SCS conditions, meanwhile the *c* single-domain state (yellow pentagram) is obtained under high SCS conditions, no matter that the SCS condition is anisotropic or isotropic. But the *r* single-domain state (orange four-pointed star), which is not obtained in the previous works, can be stable under the isotropic SCS condition in our work. That is because that under the isotropic SCS condition, surface charges on each surface are compensated to reduce the

depolarization field in each direction. Moreover, the dependence of the paraelectric–ferroelectric transition temperature on the screening factor is found similar in the previous anisotropic case and our isotropic case.

3.3 Phase diagrams and evolution of domain patterns during processes of increasing and decreasing SCS

In the following section of simulations, the effect of SCS condition at fixed temperatures is investigated. Specifically, we depict the phase diagrams in the processes of increasing and decreasing SCS at fixed temperatures in Fig. 5a and b, respectively. From the phase diagrams, one can see that, under low SCS, the rhombohedral vortex state (blue triangle) is quite stable in the nanodot and there are relatively few domain patterns in this region of phase diagrams. In contrast, under high SCS, the domain structure in the nanodot can be effectively controlled by the SCS, leading to fruitful domain patterns in this region of phase diagrams.

As shown in Fig. 5a, in the process of increasing SCS, the initial polarization distribution is obtained in the CD process under the ideal OC condition. Thus, all initial domain patterns in the process of increasing SCS are the rhombohedral vortex states (blue triangle). At $T = 0$ K and $T = 50$ K, with the increase in SCS, the orthorhombic-like vortex state (red triangle) forms in the nanodot. Moreover, the screening factor at which this phase transition occurs is 0.2 and 0.19 at $T = 0$ K and $T = 50$ K, respectively. With the further increase in SCS ($\beta < 0.2$), the orthorhombic-like vortex state maintains stability at $T = 0$ K even when the ideal SC condition is reached. Meanwhile, at $T = 50$ K the orthorhombic-like vortex state would keep stable in the range of $0 < \beta < 0.2$ and finally transforms into r single-domain state (solid four-pointed star) under the ideal SC condition. At $T = 100$ K and $T = 150$ K, as SCS increases from zero ($\beta = 1$), the rhombohedral vortex state (blue triangle) stable near the OC condition ($\beta = 1$) transforms into the orthorhombic-like vortex state (red triangle) at $\beta = 0.2$ and $\beta = 0.07$, respectively. At $T = 100$ K, with a further increase in SCS ($0.02 \leq \beta \leq 0.2$), the orthorhombic-like vortex state (red triangle) maintains stability in the nanodot. Only when SCS increases to near SC condition (i.e., $\beta = 0.01$), the orthorhombic-like vortex state transforms into the r single-domain state (solid four-pointed star). And the r single-domain state is stable under the ideal SC condition in the nanodot. At $T = 150$ K, the orthorhombic-like vortex state is stable in the nanodot under the condition of β between 0.07 and 0.03. As SCS further increases to $\beta = 0.02$, the domain pattern (green triangle ring) which has shown its details (i.e., $x = 0$, $y = 0$ planes) in Fig. 5 forms in the nanodot. With a further increase in SCS (i.e., $\beta \leq 0.01$), the r single-domain state (solid four-pointed star) forms and maintains stability at the ideal SC condition. At $T = 200$ K, the rhombohedral

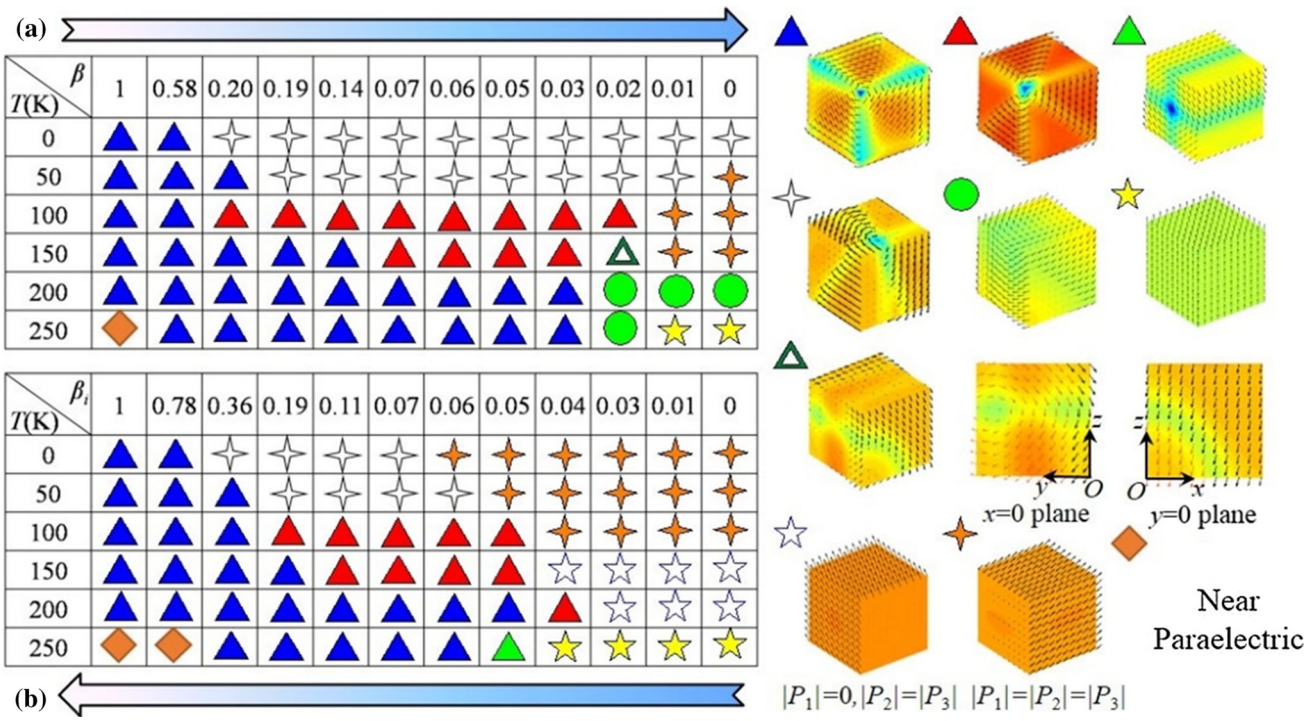

Fig. 5 Phase diagrams of equilibrium domain pattern as a function of temperature and charge screening of a nanodot during the processes of **a** decreasing (i.e., from $\beta = 1$ to $\beta = 0$) and **b** increasing (from $\beta = 0$ to $\beta = 1$) surface charge screening at different temperatures

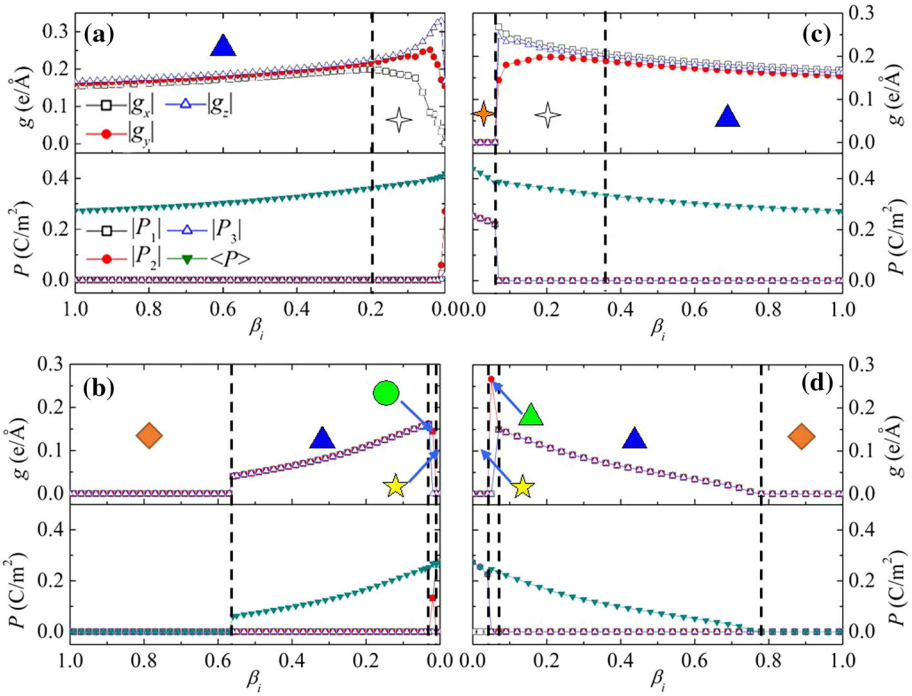

Fig. 6 Evolution of the toroidal moment, polarization and domain pattern of a nanodot during a process of increasing surface charge screening at typical temperatures (**a**) $T = 0$ K and (**b**) $T = 250$ K, and during a process of decreasing surface charge screening at (**c**) $T = 0$ K and (**d**) $T = 250$ K

vortex state (blue triangle) keeps stable in the nanodot until $\beta = 0.02$. When SCS increases to $\beta = 0.02$, the domain pattern of the nanodot transforms into a state with coexistence of both net polarization and toroidal moment (green circle, indicating a polar-vortex state), which can be further demonstrated in Fig. 6 with nonzero polarization and toroidal moment. This polar-vortex state keeps in the nanodot even under the ideal SC condition. At $T = 250$ K, the nanodot is in paraelectric phase under low SCS conditions (i.e., $\beta > 0.58$). As the SCS increases, paraelectric–ferroelectric transition happens at $\beta = 0.58$ and the rhombohedral vortex state (blue triangle) forms in the nanodot. This rhombohedral vortex state (blue triangle) maintains in the nanodot until the SCS increases to $\beta = 0.03$. When SCS reaches $\beta = 0.02$, the above-mentioned polar-vortex domain (green circle) forms in the nanodot. With a further increase in SCS ($\beta < 0.02$), the c single-domain state (yellow pentagram) forms and keeps stable in the nanodot.

The phase diagram of equilibrium domain patterns during the process of decreasing SCS shown in Fig. 5b has different features from that of the process of increasing SCS. At $T = 0$ K and $T = 50$ K, the initial r single-domain state (solid four-pointed star) maintains stability under high SCS condition and transforms into a vortex domain state (hollow four-pointed star) at $\beta = 0.07$ and $\beta = 0.06$, respectively. Then, with a further decrease in SCS, this vortex domain state maintains stability until $\beta > 0.78$ at 0 K (and $\beta > 0.36$ at 50 K), and it transforms into the rhombohedral vortex state (blue triangle). This vortex state keeps stable as the SCS condition approaches the ideal OC condition. Moreover, at $T = 100$ K, r single-domain state is found stable in the nanodot under the high SCS condition ($\beta < 0.04$). Then, the domain pattern in the nanodot transforms from the r single-domain state to the orthorhombic-like vortex state (red triangle) when SCS decreases to $\beta = 0.05$. This orthorhombic-like vortex state maintains stability in the nanodot with a further decrease in SCS ($0.05 < \beta < 0.36$). At $\beta = 0.36$, the orthorhombic-like vortex state transforms into the rhombohedral vortex state (blue triangle), and this rhombohedral vortex state is found stable in the process of further decreasing SCS ($0.36 < \beta \leq 1$). At $T = 150$ K, ac single-domain state (white pentagram) forms at high SCS ($\beta \leq 0.04$) and transforms into the orthorhombic-like vortex state (red triangle) when SCS decreases to 0.05. The orthorhombic-like vortex state maintains stability in the nanodot at $0.05 < \beta < 0.19$ and would transform into rhombohedral vortex state (blue triangle) when $0.19 < \beta < 1.0$. The evolution path at $T = 200$ K is similar to the one at $T = 150$ K, yet with different stability of the domain patterns with respect to the SCS extent (particularly the orthorhombic-like vortex state). At a high temperature of $T = 250$ K, c single-domain state (yellow pentagram) maintains in the nanodot when SCS is below 0.05. As SCS condition changes from $\beta = 0.05$ to the ideal OC condition, transformations from the c single-domain state to the tetragonal vortex state ($\beta = 0.05$), from the tetragonal vortex state to the rhombohedral vortex state ($\beta = 0.06$) and from the rhombohedral vortex state to paraelectric state ($\beta = 0.36$) are subsequently observed.

In Fig. 6a and c, we make a further analysis on the evolution paths of domain patterns during the processes of increasing and decreasing SCS at $T = 0$ K, respectively. During the increasing SCS process shown in Fig. 6a, the toroidal moment components are nonzero and keeps equal to each other when $0.2 < \beta \leq 1$. It indicates that the rhombohedral vortex state (blue triangle) maintains in the nanodot. With a further increase in SCS ($\beta \leq 0.2$), the toroidal moment components becomes different in magnitudes, as another vortex domain pattern (hollow four-pointed star) forms in the nanodot. This vortex domain pattern keeps stable in the nanodot until the ideal SC condition is reached. During the process of decreasing SCS (Fig. 6c), when the SCS is high ($0 \leq \beta \leq 0.06$), all the polarization components are nonzero, and the toroidal moment is zero, since the *r* single-domain state (solid four-pointed star) maintains stability in the nanodot. When SCS decreases to 0.07, the polarization drops to null and the toroidal moment components become nonzero and are different in magnitudes. This happens due to the transformation from the *r* single-domain state to a vortex domain pattern (hollow four-pointed star). With a further increase in SCS ($\beta > 0.36$), the toroidal moment components become equal, as the vortex domain pattern (hollow four-pointed star) in the nanodot transforms into the rhombohedral vortex state (blue triangle).

The evolution paths during the processes of decreasing and increasing SCS at $T = 250$ K are also shown in Fig. 6b and d. During the process of decreasing SCS shown in Fig. 6b, the paraelectric–ferroelectric transition happens near $\beta = 0.58$, and rhombohedral vortex state (blue triangle) forms in the nanodot. With a further increase in SCS ($0.03 \leq \beta \leq 0.58$), the toroidal moment components increase gradually and keep equal, as the rhombohedral vortex state (blue triangle) maintains stability in the nanodot. With a further increase in SCS ($\beta = 0.02$), $|g_x|$ and $|g_y|$ keep large values and $|g_z|$ drops to null. Meanwhile, $|P_1|$ and $|P_3|$ increase to nonzero values, indicating that the mentioned polar-vortex state (green circle) forms in the nanodot. When SCS increases to $\beta = 0.01$ and ideal SC condition, the toroidal moment becomes null and *c* single-domain state (yellow pentagram) forms in the nanodot. As shown in Fig. 6b, in the process of decreasing SCS, the toroidal moment and the polarization components (i.e., $|P_1|$ and $|P_2|$) keep zero and $|P_3|$ keeps nonzero at high SCS conditions ($0 \leq \beta \leq 0.04$). At this region, *c* single-domain state maintains stability in the nanodot. As the SCS increases to $\beta = 0.05$, $|g_y|$ becomes nonzero while $|P_3|$ drops to zero, indicating the tetragonal vortex state (green triangle) forms in the nanodot. With a further increase in SCS ($0.06 \leq \beta < 0.78$), the toroidal moment components become nonzero and equal to each other. Meanwhile, the polarization keeps null, indicating that the rhombohedral vortex state maintains stability in the nanodot. In this region, the toroidal moment decreases with the increase in SCS, and it becomes null at $\beta = 0.78$ as the paraelectric–ferroelectric transition happens.

3.4 Conclusions

In summary, a free-standing ferroelectric nanodot is employed as a model to investigate the combining effects of isotropic SCS condition and temperature. In order to systematically study its controllability of domain structure evolution, four typical types of experimental processes have been considered and simulated. In the first two main processes, the domain patterns and their evolution paths are obtained under different SCS conditions by varying the temperature. From the phase diagrams in these CD and HU processes, twelve kinds of domain structures are obtained. In other two main processes, nine kinds of domain patterns have been obtained by varying the SCS condition under different temperatures. These various domain patterns are linked by fruitful evolution paths. The results therefore show that the domain structure and the evolution paths in the nanodot can be effectively controlled by the SCS condition. For actual application, the extent of SCS can be controlled by the chemical environment. Thus, the domain structures in the nanodot are sensitive to the chemical environment. This indicates the potential applications in the vortex domain-based sensors. Moreover, the abundant domain patterns can be applied to the design of multistate memories. The simulations show that domain patterns can exist stably and can be controlled in the ferroelectric nanodot as small as $4 \times 4 \times 4$ nm^3, which should be promising for device miniaturization.

Acknowledgements The authors acknowledge the financial support of the National Natural Science Foundation of China (NSFC) (Nos. 11474363, 11232015, 11472313 and 11572355). Yue Zheng also thanks support from the Fundamental Research Funds for the Central Universities, Special Program for Applied Research on Super Computation of the NSFC-Guangdong Joint Fund, Fok Ying Tung Foundation and Guangdong Natural Science Funds for Distinguished Young Scholar.

References

1. R. Kretschmer, K. Binder, Phys. Rev. B **20**, 1065 (1979)
2. K. Ishikawa, K. Yoshikawa, N. Okada, Phys. Rev. B **37**, 5852 (1988)
3. M.D. Glinchuk, E.A. Eliseev, V.A. Stephanovich, Physica B Condens. Matter **322**, 356 (2002)
4. W.Y. Shih, W.-H. Shih, I.A. Aksay, Phys. Rev. B **50**, 15575 (1994)
5. G.B. Stephenson, K.R. Elder, J. Appl. Phys. **100**(17), 051601 (2006)

6. C. Thompson, D.D. Fong, R.V. Wang, F. Jiang, S.K. Streiffer, K. Latifi, J.A. Eastman, P.H. Fuoss, G.B. Stephenson, Appl. Phys. Lett. **93**(3), 182901 (2008)
7. J. Junquera, P. Ghosez, Nature **422**, 506 (2003)
8. N. Sai, A.M. Kolpak, A.M. Rappe, Phys. Rev. B **72**(4), 020101 (2005)
9. Y. Umeno, B. Meyer, C. Elsässer, P. Gumbsch, Phys. Rev. B **74**, 060101 (2006)
10. W.A. Al-Saidi, A.M. Rappe, Phys. Rev. B **82**, 155304 (2010)
11. D.D. Fong, A.M. Kolpak, J.A. Eastman, S.K. Streiffer, P.H. Fuoss, G.B. Stephenson, C. Thompson, D.M. Kim, K.J. Choi, C.B. Eom, Phys. Rev. Lett. **96**, 127601 (2006)
12. M.J. Highland, T.T. Fister, M.-I. Richard, D.D. Fong, P.H. Fuoss, C. Thompson, J.A. Eastman, S.K. Streiffer, G.B. Stephenson, Phys. Rev. Lett. **105**, 167601 (2010)
13. J. Shin, V.B. Nascimento, G. Geneste, J. Rundgren, E.W. Plummer, B. Dkhil, S.V. Kalinin, A.P. Baddorf, Nano Lett. **9**, 3720 (2009)
14. Y. Kim, I. Vrejoiu, D. Hesse, M. Alexe, Appl. Phys. Lett. **96**, 202902 (2010)
15. I.I. Naumov, L. Bellaiche, H. Fu, Nature **432**, 737 (2004)
16. I. Ponomareva, I.I. Naumov, L. Bellaiche, Phys. Rev. B **72**, 214118 (2005)
17. S. Prosandeev, L. Bellaiche, Phys. Rev. B **75**, 094102 (2007)
18. S. Prosandeev, I. Ponomareva, I. Kornev, L. Bellaiche, Phys. Rev. Lett. **100**, 047201 (2008)
19. S. Prosandeev, L. Bellaiche, Phys. Rev. Lett. **101**, 097203 (2008)
20. Y. Su, J.N. Du, Appl. Phys. Lett. **95**, 012903 (2009)
21. J. Wang, M. Kamlah, Appl. Phys. Lett. **93**, 042906 (2008)
22. W.J. Chen, Y. Zheng, B. Wang, Appl. Phys. Lett. **100**, 062901 (2012)
23. W.J. Chen, Y. Zheng, B. Wang, J.Y. Liu, J. Appl. Phys. **115**, 214106 (2014)
24. W.J. Chen, Y. Zheng, Acta Mater. **88**, 41 (2015)
25. Y.L. Li, S.Y. Hu, Z.K. Liu, L.Q. Chen, Appl. Phys. Lett. **81**, 427 (2002)
26. G.B. Stephenson, M.J. Highland, Phys. Rev. B **84**, 064107 (2011)
27. M.J. Highland, T.T. Fister, D.D. Fong, P.H. Fuoss, C. Thompson, J.A. Eastman, S.K. Streiffer, G.B. Stephenson, Phys. Rev. Lett. **107**, 187602 (2011)
28. D.C. Ma, Y. Zheng, B. Wang, C.H. Woo, Appl. Phys. Lett. **99**, 142908 (2011)
29. C.M. Wu, W.J. Chen, D.C. Ma, C.H. Woo, Y. Zheng, J. Appl. Phys. **112**, 104108 (2012)
30. C.M. Wu, W.J. Chen, Y. Zheng, D.C. Ma, B. Wang, J.Y. Liu, C.H. Woo, Sci. Rep. **4**, 3946 (2014)
31. M.J. Haun, E. Furman, S.J. Jang, H.A. McKinstry, L.E. Cross, J. Appl. Phys. **62**, 3331 (1987)
32. Y.L. Li, L.E. Cross, L.Q. Chen, J. Appl. Phys. **98**, 064101 (2005)
33. W.J. Chen, Y. Zheng, B. Wang, D.C. Ma, F.R. Ling, Phys. Chem. Chem. Phys. **15**, 7277 (2013)
34. C.H. Woo, Y. Zheng, Appl. Phys. A Mater. Sci. Process. **91**, 59 (2008)
35. Y. Zheng, C.H. Woo, Appl. Phys. A Mater. Sci. Process. **97**, 617 (2009)
36. J. Wang, T.Y. Zhang, Phys. Rev. B. **73**, 144107 (2006)
37. T. Sluka, A.K. Tagantsev, D. Damjanovic, M. Gureev, N. Setter, Nat. Commun. **3**, 748 (2012)
38. J. Hlinka, P. Márton, Phys. Rev. B **74**, 104104 (2006)
39. W.L. Zhong, Y.G. Wang, P.L. Zhang, B.D. Qu, Phys. Rev. B **50**, 698 (1994)
40. $\alpha_1 = 4.124(T - 388) \times 10^5$, $\alpha_{11} = -2.097 \times 10^8$, $\alpha_{12} = 7.974 \times 10^8$, $\alpha_{111} = 1.294 \times 10^9$, $\alpha_{112} = -1.950 \times 10^9$, $\alpha_{123} = -2.500 \times 10^9$, $\alpha_{1111} = 3.863 \times 10^{10}$, $\alpha_{1112} = 2.529 \times 10^{10}$, $\alpha_{1122} = 1.637 \times 10^{10}$, $\alpha_{1123} = 1.367 \times 10^{10}$, $Q_{11} = 0.1104$, $Q_{12} = -0.0452$, $Q_{44} = 0.0289$, $c_{11} = 27.5 \times 10^{10}$, $c_{12} = 17.9 \times 10^{10}$, $c_{44} = 5.43 \times 10^{10}$, $G_{11} = 51 \times 10^{-11}$, $G_{12} = 0$, $G_{44} = G'_{44} = 1 \times 10^{-11}$, $\delta_i^{\text{eff}} = 43 \times 10^{-9}$ and $\varepsilon_b \approx 4.425 \times 10^{-10}$ (SI units and T in K)
41. S. Prosandeev, I. Ponomareva, I. Naumov, I. Kornev, L. Bellaiche, J. Phys. Condens. Matter **20**, 193201 (2008)